USGS
science for a changing world

Petrographic, Geochemical, and Geochronologic Data for Cenozoic Volcanic Rocks of the Tonopah, Divide, and Goldfield Mining Districts, Nevada

Data Series 1099

U.S. Department of the Interior
U.S. Geological Survey

Cover. View to the west from Preble Mountain, Goldfield district. Pittsburgh-Goldfield mine dump in the middle foreground; town of Goldfield and the productive part of the district are beneath the near-horizontal volcanic rocks that form a dark layer below the skyline. Photograph by Edward A. du Bray, U.S. Geological Survey, 2012.

Petrographic, Geochemical, and Geochronologic Data for Cenozoic Volcanic Rocks of the Tonopah, Divide, and Goldfield Mining Districts, Nevada

By Edward A. du Bray, David A. John, Peter G. Vikre, Joseph P. Colgan, Michael A. Cosca, Leah E. Morgan, Robert J. Fleck, Wayne R. Premo, and Christopher S. Holm-Denoma

Data Series 1099

U.S. Department of the Interior
U.S. Geological Survey

U.S. Department of the Interior
DAVID BERNHARDT, Secretary

U.S. Geological Survey
James F. Reilly II, Director

U.S. Geological Survey, Reston, Virginia: 2019

Suggested citation:
du Bray, E.A., John, D.A., Vikre, P.G., Colgan, J.P., Cosca, M.A., Morgan, L.E., Fleck, R.J., Premo, W.R., and Holm-Denoma, C.S., 2019, Petrographic, geochemical, and geochronologic data for Cenozoic volcanic rocks of the Tonopah, Divide, and Goldfield mining districts, Nevada: U.S. Geological Survey Data Series 1099, 15 p., https://doi.org/10.3133/ds1099.

ISSN 2327-638X (online)

Acknowledgments

Supplemental geologic mapping and sample collection for this study were conducted as part of the Magmatic-Tectonic History and Component Sources of Major Precious Metal Deposits at Tonopah and Goldfield, Nevada Project funded by the U.S. Geological Survey Mineral Resources Program. We thank Lawrence J. Garside and Roger P. Ashley for providing access to samples collected during their pioneering work in the Tonopah, Divide, and Goldfield mining districts. Thanks to Matt Heizler (New Mexico Geochronological Research Laboratory) for the $^{40}Ar/^{39}Ar$ ages reported in appendix 6. Thanks also to Richard J. Moscati for help in various aspects of the U-Pb zircon geochronologic age determinations. Constructive reviews by Paul Denning and Bradley S. Van Gosen are much appreciated and helped clarify data presentation.

Contents

Figure

Tables

Petrographic, Geochemical, and Geochronologic Data for Cenozoic Volcanic Rocks of the Tonopah, Divide, and Goldfield Mining Districts, Nevada

By Edward A. du Bray, David A. John, Peter G. Vikre, Joseph P. Colgan, Michael A. Cosca, Leah E. Morgan, Robert J. Fleck, Wayne R. Premo, and Christopher S. Holm-Denoma

Introduction

The purpose of this report is to summarize geochemical, petrographic, and geochronologic data (du Bray and others, 2019) for samples, principally those of unmineralized Tertiary volcanic rocks, from the Tonopah, Divide, and Goldfield mining districts of west-central Nevada (fig. 1). Much of the data presented here for the Tonopah and Divide mining districts are for samples collected by Bonham and Garside (1979) during geologic mapping in and around those mining districts, whereas much of that for samples from the Goldfield mining district were obtained by Ashley (1974; 1979; 1990a). Additional data were derived from samples collected 2012–17, as part of the U.S. Geological Survey Mineral Resources Program funded project titled, "Magmatic-tectonic history and component sources of major precious metal deposits in the southern Walker Lane." A small amount of additional geochemical data for samples from each of the mining districts were compiled from other sources. Individual sample collectors are identified by appropriate entries in the "Collector" field (appendix 1) and published sources of geochemical data are defined by entries in the "Chem_Src" data field (appendix 1).

The geologic setting of bonanza silver-gold quartz-adularia veins in the Tonopah mining district is complex and incompletely understood. Basement rocks exposed about 10 kilometers (km) north and 15 km south of the mining district include Triassic (John and McKee, 1987) granitic rocks and the lower Paleozoic siliciclastic metasedimentary rocks of the "Nolan belt domain" (Crafford, 2007, 2008) that they intrude; these metasedimentary rocks were deposited on Precambrian rocks of the North American craton. These basement rocks are overlain by Miocene volcanic rocks that are manifestations of arc magmatism associated with the southern segment of the ancestral Cascades arc (du Bray and others, 2014). Arc magmatism in the Tonopah mining district was extinguished by northward migration of the Mendocino triple junction and the transition to a transform plate margin in this region at about 12 mega-annum (Ma). Lava flows and lava dome complexes are volumetrically dominant, although ash-flow tuffs, including the Fraction Tuff and the Heller Tuff of Bonham and Garside (1979), are also significant within the mining district. Mineralized veins are hosted primarily by andesite and dacite lava flows and breccias of the Mizpah Trachyte near the south end of a lava dome complex (Nolan, 1935; Bonham and Garside, 1979). New argon-argon ($^{40}Ar/^{39}Ar$) dates (this report and Cosca and Morgan, 2018) suggest that rocks of the Mizpah Trachyte were erupted about 21.4 Ma. The Fraction Tuff overlies the Mizpah Trachyte. In the Tonopah mining district, the Fraction Tuff was likely deposited in an intracaldera environment and was erupted from a caldera whose northern margin is about 10 km north of Tonopah (John and others, 2015). In the area around Tonopah, the overlying Siebert Formation of Bonham and Garside (1979) may constitute a voluminous, thick, in part ash-fall deposit that accumulated in the basin formed during collapse of the caldera that erupted the Fraction Tuff and in the surrounding lowlands.

New $^{40}Ar/^{39}Ar$ dates of adularia on quartz-adularia veins in altered Mizpah Trachyte rocks range from about 20.5 to 19.9 Ma (this report and Cosca and Morgan, 2018). High-grade silver-gold deposits were mined from some of these veins. More than 174 million ounces (Moz) silver and 1.86 Moz gold were produced (mostly from 1910 to 1930). The principal ore minerals are argentite, polybasite, pyrargyrite, and electrum; other vein minerals include sphalerite, galena, chalcopyrite, pyrite, pearcite, muscovite, and calcium-manganese carbonates (Bonham and Garside, 1974; this report). Dates of the quartz-adularia veins suggest nearly simultaneous eruption of the Fraction Tuff, possible caldera formation, and vein mineralization (John and others, 2015).

Compositions of Tonopah volcanic rocks vary essentially continuously from about 60 to 78 weight percent silica (SiO_2), although rocks with ≈67 to 72 weight percent SiO_2 are somewhat under-represented. Tonopah rock compositions form a high-potassium calc-alkaline series with pronounced negative titanium-phosphorus-niobium-tantalum anomalies and high barium/niobium, barium/tantalum, and lanthanum/niobium typical of subduction-related continental margin arcs (Gill, 1981). Most Tonopah mining district rocks are

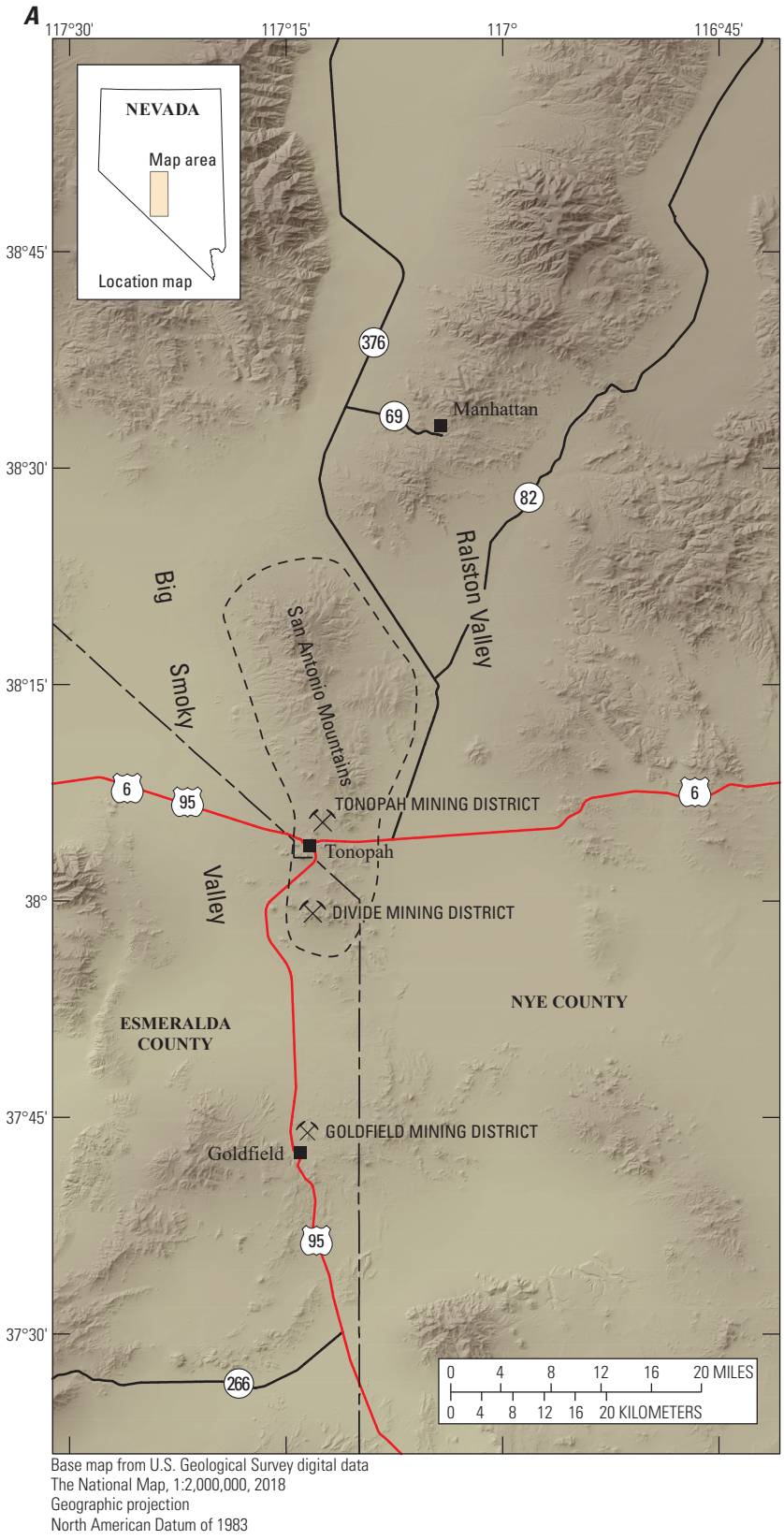

Figure 1. Location of the Tonopah, Divide, and Goldfield mining districts, Nevada. *A*, Index map of central Nevada showing the locations of the three mining districts relative to Tonopah and Goldfield. *B*, Map of northern California and western Nevada (modified from Colgan and others, 2011; John and others, 2012) showing the inferred extent of ancestral (green polygons) and modern High Cascades (cross hatched polygons) magmatic arcs.

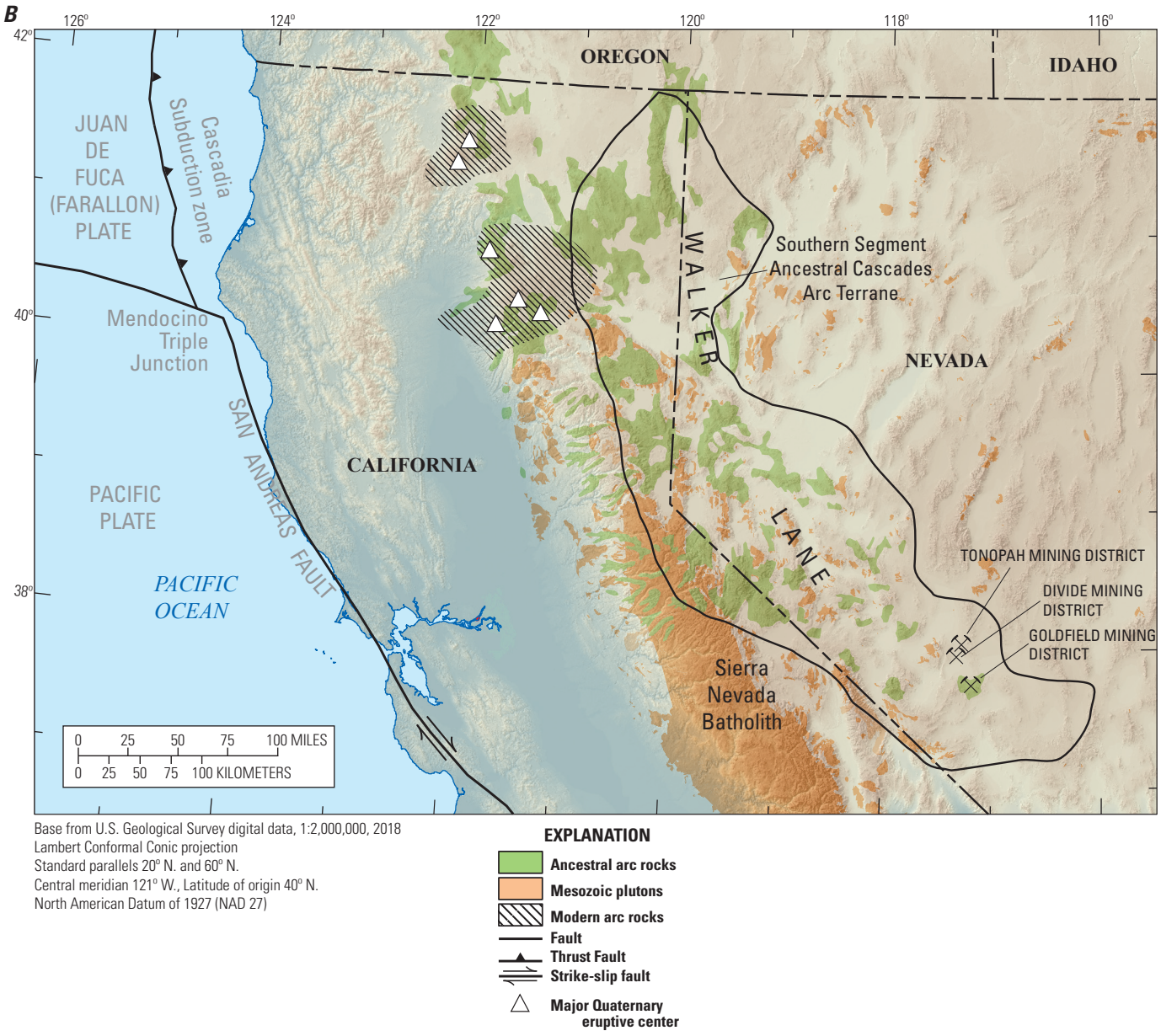

Figure 1. Location of the Tonopah, Divide, and Goldfield mining districts, Nevada. *A*, Index map of central Nevada showing the locations of the three mining districts relative to Tonopah and Goldfield. *B*, Map of northern California and western Nevada (modified from Colgan and others, 2011; John and others, 2012) showing the inferred extent of ancestral (green polygons) and modern High Cascades (cross hatched polygons) magmatic arcs.—Continued

porphyritic, commonly containing 10–35 volume percent phenocrysts principally composed of plagioclase, pyroxene, and hornblende ±biotite; quartz, alkali feldspar, or olivine are present in some samples.

The geologic setting of the silver-gold dominated Divide mining district, centered about 8 km south of Tonopah, is similar to that of the Tonopah mining district; similarly, it is dominated by Miocene volcanic rocks. Like the Tonopah mining district, basement rocks, exposed about 10 km south of the mining district, are principally lower Paleozoic siliciclastic metasedimentary rocks of the "Nolan belt domain" (Crafford, 2007, 2008) but also include a distinctive Cretaceous muscovite granite (Bonham and Garside, 1979). The Miocene volcanic rocks, also associated with ancestral Cascades arc magmatism, overlie the Paleozoic and Mesozoic basement rocks and Fraction Tuff. Mineralized veins and breccias in the Divide mining district are also hosted in Miocene volcanic rocks, principally the Oddie Rhyolite, Heller Tuff, and tuffs

of the Siebert Formation (Nolan, 1935; Bonham and Garside, 1979; Erdman and Barabas, 1996).

The eastern part of the mining district and a large area further east are dominated by additional Miocene volcanic rocks, including the Divide Andesite and the compositionally diverse volcanics of Donovan Peak. The Divide and Donovan rocks are associated with local eruptive or intrusive centers and consist of lava flows, lava dome complexes, and hypabyssal plugs. These rocks may represent resurgent magmatism associated with the southern of two hypothesized calderas in the Tonopah area. New $^{40}Ar/^{39}Ar$ dates (this report and Cosca and Morgan, 2018) indicate that shallowly emplaced Oddie Rhyolite domes were intruded between about 17.3 and 16.6 Ma. Potassium-argon (K-Ar) dates of air-fall tuffs of the Siebert Formation in the Tonopah area are poorly constrained between about 20 and 16 Ma (Bonham and Garside, 1979). New $^{40}Ar/^{39}Ar$ ages (this report and Cosca and Morgan, 2018) for these volcaniclastic rocks provide little clarity concerning the age of these deposits because feldspars and other minerals contained therein represent diverse, multiage sources. New $^{40}Ar/^{39}Ar$ dates (this report and Cosca and Morgan, 2018) indicate that ages for the Divide Andesite and volcanics of Donovan Peak are 17.6 to 17.4 and 17.3 to 16.5 Ma, respectively.

Existing K-Ar dates for a variety of mineralized samples from the Divide mining district suggest that mineralization occurred between about 16.4 and 15.3 Ma (Bonham and Garside, 1979), whereas new $^{40}Ar/^{39}Ar$ dates of adularia indicates ore formation between about 17.0 and 16.8 Ma. Quartz-adularia epithermal deposits in the Divide mining district consist of silver-dominated vein and breccia deposits from which about 3.7 Moz. silver and 0.04 Moz. gold were produced (Erdman and Barabas, 1996); the principal ore mineral in the mining district was cerargyrite although sphalerite, argentiferous galena, chalcopyrite, molybdenite, electrum, acanthite, pyrargyrite, and possible tetrahedrite have been identified in dump samples (Bonham and Garside, 1974; Graney, 1987; Erdman and Barabas, 1996).

Divide mining district volcanic rocks contain ≈61 to 77 weight percent SiO_2. Rock compositions form a high-potassium calc-alkaline series with geochemical characteristics typical of subduction-related continental margin arcs (Gill, 1981). Many of the Divide mining district rocks are distinctly more alkaline, particularly sodic, than volcanic rocks in either the Tonopah or Goldfield mining districts. Most Divide mining district rocks are porphyritic, commonly containing 5–25 volume percent phenocrysts principally composed of plagioclase, biotite, and hornblende; quartz and alkali feldspar are present in samples of the more silicic units, especially the Oddie Rhyolite.

The geology of the Goldfield mining district is dominated by intensely quartz-alunite-altered Miocene volcanic and pre-Tertiary rocks (Vikre and Henry, 2011), including lower Paleozoic siliciclastic metasedimentary rocks, the "Nolan belt domain" of Crafford (2007, 2008), which were deposited on Precambrian rocks of the North American craton. These basement rocks, exposed mostly in deeper mine workings, were intruded by Jurassic granitic rocks (this report). The volcanic rocks are principally lava flows but also include breccias and lava domes. Miocene and minor Oligocene volcanic rocks in the Goldfield mining district constitute the southernmost extent of magmatism associated with the southern segment of the ancestral Cascades arc (du Bray and others, 2014). Northward migration of the Mendocino triple junction terminated arc magmatism in the Goldfield mining district at about 12.9 Ma. These volcanic rocks at Goldfield are cut by a dense network of west-northwest and north-northeast trending normal faults. Milltown Andesite lava flows are the volumetrically dominant volcanic rocks in the Goldfield mining district; a K-Ar date indicates that the andesite was erupted about 21.5 ± 0.5 Ma (Albers and Stewart, 1972), whereas several new $^{40}Ar/^{39}Ar$ dates (this report and Cosca and Morgan, 2018) indicate an age of about 22.3 to 21.9 Ma. Other important units in the Goldfield mining district include unnamed porphyritic andesite lava flows and domes, latite (Ransome, 1909), and small-volume rhyolite masses. Several new $^{40}Ar/^{39}Ar$ dates (this report and Cosca and Morgan, 2018) of the porphyritic andesite are 22.4 to 21.8 Ma. Ashley (1990a) suggests that silicic ash-flow tuffs (the Vindicator Rhyolite and the Morena Rhyolite of Ransome, 1909) represent eruptions from a 6-km diameter caldera delineated by a series of poorly defined, presumed ring fractures. However, geophysical data suggest that these fractures are not related to caldera formation but to pluton emplacement (Blakely and others, 2007). A new $^{40}Ar/^{39}Ar$ date of sanidine indicates eruption of the Morena Rhyolite of Ransome (1909) at 25.17 ± 0.03 Ma (this report and Cosca and Morgan, 2018). New $^{40}Ar/^{39}Ar$ dates of biotite and sanidine in rhyolite of Wildhorse Spring in the eastern part of the mining district indicate eruption between 22.2 and 21.5 Ma (this report and Cosca and Morgan, 2018). A series of younger, middle Miocene mafic lava flows overlie mineralized, lower Miocene rocks in the Goldfield mining district.

Miocene and minor Oligocene volcanic rocks in the Goldfield mining district contain numerous, fault breccia-hosted quartz-alunite epithermal deposits (Vikre and Henry, 2011) from which 4.19 Moz of gold and 1.45 Moz of silver were produced (Albers and Stewart, 1972). New $^{40}Ar/^{39}Ar$ dates (this report and Cosca and Morgan, 2018) of alunite in breccias and altered volcanic rocks range from 22.4 to 7.0 Ma though most dates cluster between 21.9 to 21.2 Ma. Abundant mineralized fault breccia masses are localized in a 40 (km^2) area within which acidic hydrothermal fluids intensely altered Miocene, and minor Oligocene volcanic and pre-Tertiary rocks, to advanced argillic mineral assemblages (Ashley, 1990a; Vikre and Henry, 2011). Within this area, quartz-rich fault breccias form resistant zones or ledges enclosed within recessively weathered, quartz-poor, alunite- or pyrophyllite-rich rocks (Ransome, 1909; Ashley and Albers, 1975, Ashley, 1990a).

Most Goldfield mining district volcanic rocks contain between ≈54 and 69 weight percent SiO_2; andesitic and dacitic compositions are dominant. Like volcanic rocks in the Tonopah mining district, those in the Goldfield mining district form a high-potassium, calc-alkaline series with pronounced negative titanium-phosphorus-niobium-tantalum anomalies and high

barium/niobium typical of subduction-related continental margin arcs (Gill, 1981). These rocks are porphyritic and contain 15–35 volume percent phenocrysts principally composed of plagioclase, pyroxene, hornblende, and biotite.

Analytical Methods

Standard petrographic microscope techniques were employed to identify phenocryst minerals and estimate their relative abundances in 468 volcanic rock samples from the Tonopah, Divide, and Goldfield mining districts (appendix 2; see Data Fields section). In addition, phenocryst size and crystallinity, rock textures, groundmass characteristics, and accessory mineral assemblages were recorded for each sample.

New whole-rock chemical analyses of 190 samples, most collected between 2012 and 2017, were conducted in analytical laboratories of SGS Minerals, Toronto, Canada (appendix 3; see Data Fields section). Major oxide abundances (recalculated to 100 percent, volatile free) were determined by wavelength dispersive X-ray fluorescence spectrometry. A 55-element method that uses a combination of inductively coupled plasma-atomic emission spectrometry and inductively coupled plasma-mass spectrometry was used to determine trace element abundances. These chemical data are also archived in the National Geochemical Database (NGDB) of the U.S. Geological Survey. Pertinent analytical methods are described by Taggart (2002). Compositions of an additional 108 samples of Tonopah, Divide, and Goldfield mining district rocks, from published and unpublished sources, are also included in this data compilation. These samples were analyzed by different laboratories employing diverse analytical techniques, which resulted in data of variable quality for a highly variable set of components. Laboratories, techniques, and the analyzed constituents are documented in the sources (identified in appendix 1; see Data Fields section) from which these data were compiled.

Although efforts were made to collect only unaltered samples, a review of the available geochemical data indicated that some of the analyzed samples were affected by post-magmatic hydrothermal alteration. Samples with any of the following characteristics are considered to be altered: SiO_2 abundances greater than 78 weight percent, volatile (loss on ignition) content greater than 4 weight percent (excluding hydrated vitrophyres), sodium oxide (Na_2O) abundances less than 1 weight percent, or Na_2O/K_2O less than 0.5. Primary igneous rock compositions of samples with any of these characteristics probably have not been preserved; these samples and the type of alteration they experienced are identified in appendix 3.

New $^{40}Ar/^{39}Ar$ ages (appendixes 4–7) provide temporal constraints on volcanic and hydrothermal activity in the Tonopah, Divide, and Goldfield mining districts. Volcanic rocks were dated using either separates of one or more phenocryst minerals (plagioclase, sanidine, biotite, and amphibole) or whole-rock aggregates. Ages of hydrothermal alteration were determined using alunite or adularia separates.

Samples collected for $^{40}Ar/^{39}Ar$ analysis were most commonly crushed and sieved to sizes appropriate for preparation of high-purity separates. Mineral separations were made using standard magnetic and heavy-liquid separation techniques. Whole-rock samples were prepared by crushing and isolating rock fragments of ~1 cubic millimeter (mm^3) from fresh rock free of obvious alteration and xenocrysts. Analyzed samples were washed in deionized water. In many cases, final separates were prepared by hand picking individual crystals.

The $^{40}Ar/^{39}Ar$ ages reported in appendixes 4 and 5 (Cosca and Morgan, 2018) were determined in the U.S. Geological Survey $^{40}Ar/^{39}Ar$ Laboratory in Denver, Colorado. Samples, together with standards, were irradiated in several separate experiments of either 5 or 7 megawatt hours in the central thimble position of the U.S. Geological Survey TRIGA® Reactor Facility in Denver, Colorado. Carbon dioxide (CO_2) laser fusion of >10 individual Fish Canyon Tuff sanidine crystals (28.201 ± 0.09 Ma; Kuiper and others, 2008) at closely monitored positions within the irradiation package resulted in neutron flux ratios reproducible to ± 0.25% (2σ). Cadmium shielding during irradiation prevented any measurable nucleogenic ($^{40}Ar/^{39}Ar$) potassium (K). Isotopic production ratios and interfering nucleogenic reactions were determined from irradiated calcium fluoride (CaF_2) and zero age K-silicate glass, and for this study the following values were measured: $(^{36}Ar/^{37}Ar)Ca = (2.77 \pm 0.03) \times 10^{-4}$; $(^{39}Ar/^{37}Ar)Ca = (6.54 \pm 0.33) \times 10^{-4}$; and $(^{38}Ar/^{39}Ar)K = (1.29 \pm 0.03) \times 10^{-2}$. The irradiated samples and standards were loaded into known positions of a stainless steel planchette, placed into a chamber and sealed by an externally pumped zinc selenide window, and evacuated to ultrahigh vacuum conditions within a fully automated stainless steel extraction line designed and built at the USGS in Denver, Colorado. A 50 watt (W) CO_2 laser equipped with a beam homogenizing lens was used to incrementally heat and (or) fuse mineral grains and rock fragments. The liberated gas was expanded and purified by exposure to a cryogenic trap maintained at −135 ºC and to two SAES GP50® getters, one operated at 0 amps and one operated at 2.2 amps. Following purification, sample gas was expanded online into a Thermo Scientific ARGUS VI® mass spectrometer and Ar isotopes were measured simultaneously using faraday detectors (Ar masses 37–40) and ion counting (Ar mass 36). Blanks and sample data were acquired during 10 measurement cycles and time zero intercepts were determined by best-fit linear and (or) polynomial regressions to the data. The data were corrected for mass discrimination, blanks, radioactive decay, and interfering nucleogenic reactions and $^{40}Ar/^{39}Ar$ ages were calculated with the decay constants of Min and others (2000) and a $^{40}Ar/^{36}Ar$ ratio of trapped argon equal to the atmospheric value of 298.56 (Lee and others, 2006). Data collection and age calculations were conducted using the Masspec software program written by A. Deino of the Berkeley Geochronology Center.

The $^{40}Ar/^{39}Ar$ ages reported in appendix 6 were determined in the New Mexico Geochronological Research Laboratory. Analytical methods are described by Heizler (2003, 2005).

The $^{40}Ar/^{39}Ar$ ages reported in appendix 7 were determined in the U.S. Geological Survey $^{40}Ar/^{39}Ar$ laboratory in Menlo Park, California. Samples were crushed and sieved to sizes appropriate for preparation of high-purity alunite separates. In many cases, final separates were prepared by hand picking individual crystals. Samples were irradiated in the U.S. Geological Survey TRIGA Reactor Facility in Denver, Colorado; irradiation times were between 10 and 16 hours. Determined ages were obtained by laser-fusion analysis, whereby grains were fused with a CO_2 laser in a single heating step (appendix 7). One or several grains were used in each analysis, depending on grain size. In all cases, a minimum number of grains were used to permit recognition and elimination of most xenocrystic or detrital contamination through identification of outliers. The reported age for laser-fusion analyses represents the weighted mean of the replicate analyses, with the inverse variance of propagated, within-run (internal) errors of each used as its weighting factor (Taylor, 1982). Sanidine from the Fish Canyon Tuff, with an age of 28.198 Ma, was used for calculation of neutron flux. Decay and abundance constants are those recommended by Steiger and Jäger (1977). Ages were calculated assuming a $^{40}Ar/^{36}Ar$ ratio of trapped argon equal to the atmospheric value of 295.5.

Zircons were separated from crushed and ground samples using standard magnetic and heavy liquid techniques, hand picked under a binocular microscope, and mounted in epoxy discs. Zircons were analyzed by Sensitive High Resolution Ion Microprobe with Reverse-Geometry (SHRIMP-RG) at Stanford University and by laser ablation inductively coupled mass spectrometry (LA-ICPMS) in the U.S. Geological Survey Southwest Isotope Research Laboratory in Denver, Colorado (Colgan, 2018).

For the SHRIMP analyses, zircon mounts were ground to expose grain interiors, polished, and imaged with cathodoluminescence (CL) on a JEOL 5600 SEM® to identify internal structure (rims, core, and so forth). The SHRIMP-RG was operated with an oxygen (O_2^-)-primary ion beam that varied in intensity from 4.0 to 5.5 nA, with a typical spot diameter of 20–25 micrometers (μm). Zircon surfaces were rastered by the primary beam for 120–180 seconds before data was collected. For all samples, the following peaks were measured sequentially: ^{89}Y, $^{139}La^+$, $^{140}Ce^+$, $^{146}Nd^+$, $^{147}Sm^+$, $^{153}Eu^+$, $^{155}Gd^+$, $^{163}Dy^{16}O^+$, $^{166}Er^{16}O^+$, $^{172}Yb^{16}O^+$, $^{90}Zr_2{}^{16}O^+$, $^{180}Hf^{16}O^+$, $^{204}Pb^+$, a background measured at 0.045 mass units above the $^{204}Pb^+$ peak, $^{206}Pb^+$, $^{207}Pb^+$, $^{208}Pb^+$, $^{232}Th^+$, $^{238}U^+$, $^{232}Th^{16}O^+$, $^{238}U^{16}O^+$, and $^{238}U^{16}O_2{}^+$. Mounts were analyzed with 4–5 scans (peak-hopping cycles in mass order) and measurements were made at mass resolutions of $M/\Delta M$ = 7,500–8,500 (10 percent peak height). Raw data were reduced using Squid 2 rev. 2.51 software (Ludwig, 2009), with corrections for background and collector dead time.

Measured $^{206}Pb/^{238}U$ was corrected using a standard U^+/Pb^+ compared to U^+/UO^+ calibration for sputtering bias (Williams, 1997). Radiogenic U-Pb ratios were derived after correction for common Pb using a ^{207}Pb correction scheme (Williams, 1997), or from measured ^{204}Pb with model common Pb compositions from Stacey and Kramers (1975). $^{238}U/^{235}U$ was assumed to be 137.88. Concentration data for U, thorium (Th) and all of the measured trace elements were standardized against zircon standard Madagascar Green (MAD) (Barth and Wooden, 2010), which had standard deviations (2σ uncertainties) of about ±3 percent for hafnium Hf, ±5–10 percent for the yttrium (Y) and heavy rare earth elements (HREE), ±10–15 percent, and up to ±40 percent for lanthanum (La). U-Pb ages were calculated relative to the R33 zircon standard (420 Ma; Black and others, 2004; Mattinson, 2010). Data (appendix 8) were reduced using methods described by Williams (1997) and Ireland and Williams (2003), using Excel and the add-in programs Isoplot3 and Squid 2 rev. 2.51 (Ludwig 2003, 2009).

Laser ablation-inductively coupled plasma analyses of igneous zircon grains were conducted using a Nu Instruments AttoM™ laser ablation, single collector, inductively coupled plasma mass spectrometer (LA-SC-ICPMS). Zircon was ablated with a Photon Machines Excite™ 193 nm ArF excimer laser in spot mode (150 total bursts for each spot analysis) with a repetition rate of 5 hertz (Hz), laser energy of ~3 milliJoule, and an energy density of 4.11 joules/square centimeter. Pit depths are typically less than 20 μm. The rate of He carrier gas flow from the HelEx™ cell of the laser was ~0.6 L/min. Makeup Ar gas (~0.2 L/min) was added to the sample stream prior to its introduction into the plasma. Nitrogen with flow rate of 5.5 milliliter/minute was added to the sample stream to allow for significant reduction in ThO^+/Th^+ (<0.5 percent) and improved the ionization of refractory Th (Hu and others, 2008). Laser spot sizes on zircon were ~25 μm. With the magnet parked at a constant mass, the flat tops of the isotope peaks of ^{202}Hg, ^{204}(Hg+Pb), ^{206}Pb, ^{207}Pb, ^{208}Pb, ^{232}Th, ^{235}U, and ^{238}U were measured by rapidly deflecting the ion beam with a 30 second on peak background measured prior to each 30 s analysis. Raw data were reduced offline using the Iolite™ 2.5 program (Paton and others, 2011) to subtract on peak background signals, correct for U-Pb downhole fractionation, and normalize the instrumental mass bias using external mineral reference materials, the ages of which had previously been determined by isotope dilution thermal ionization mass spectrometry (ID-TIMS). Ages were corrected by standard sample bracketing with the primary zircon reference material Temora2 (417 Ma; Black and others, 2004) and secondary reference material Plešovice (337 Ma, Sláma and others, 2008) and an inhouse standard WRP-63-08 (1707 Ma; W. Premo, oral commun., 2016). Reduced data were compiled into Wetherill concordia diagrams using Isoplot 4.15 (Ludwig, 2012). $^{206}Pb/^{238}U$ ages are reported for igneous zircon samples less than ~1300 Ma and $^{207}Pb/^{206}Pb$ ages are used for older ages following the recommendations of Gehrels (2012).

Standard petrographic microscope techniques and an automated point count stage were used to determine the relative proportions of various phenocryst minerals and matrix or groundmass in samples of the Fraction Tuff and Heller Tuff (appendix 10).

Data Fields

Petrographic, geochemical, and geochronologic data for volcanic rocks exposed in the Tonopah, Divide, and Goldfield mining districts are presented in columns or sets of related columns (appendixes 2–10) in Microsoft Excel 2010 workbooks (.xlsx format). The contents of appendix 1 (data fields defined in table 1) constitute basic sample characterization, including sample location, sample treatment, and lithologic characterization. Appendix 2 contains petrographic observations for each sample (data fields defined in table 2). Appendix 3 contains geochemical data for analyzed samples (data fields defined in table 3). Geochemical data in some worksheet cells may appear to be more precise than displayed values, but the implied precision is a misleading artifact of computational processes (for instance, recalculation to 100-percent volatile free) used to create data-cell contents. Blank cells in the worksheet appendixes indicate null values or that no data are available. In appendix 3 (geochemistry data), some blank cells reflect abundances that were reported as "less than the detection limit"; these values were replaced by blank cells to enable statistical analysis of the uncensored data. The results of $^{40}Ar/^{39}Ar$ age determination experiments are presented in appendixes 4–7, those for U-Pb analysis of zircon separates are presented in appendixes 8 and 9, and microscope-based point counts of Fraction Tuff and Heller Tuff samples in appendix 10.

Table 1. Definition and characterization of data fields included in appendix 1 (status and treatment of samples).

Field name	Field description
Field_ID	Field-assigned sample identifier; Field_ID entries link data for individual rows to the contents of particular rows in the other appendixes and, for U.S. Geological Survey samples, to the National Geochemical Database
District	Tonopah, Divide, or Goldfield
Collector	Sample collector initials, where EDB is E.A. du Bray, RPA is R.P. Ashley; PGV is P.G. Vikre; OTH is other (as identified in the Chem_Src field); HBLG is H.F. Bonham or L.J. Garside; DAJ is D.A. John; and MAC is M.A. Cosca
Longitude	In decimal degrees, relative to the North American Datum of 1927; locations (with four or five significant figures) are accurate within several to tens of meters, locations with three significant figures are accurate within hundreds of meters, locations with two significant figures are accurate within thousands of meters. Longitude is reported as a negative value (western hemisphere)
Latitude	In decimal degrees, relative to the North American Datum of 1927; locations with four or five significant figures are accurate within several to tens of meters, locations with three significant figures are accurate within hundreds of meters, locations with two significant figures are accurate within thousands of meters. Latitude is reported as a positive value (northern hemisphere)
Chem	X, chemical analysis for sample obtained (see appendix 3)
TS	X, thin section of sample prepared and examined using a petrographic microscope (see appendix 2)
REF	X, reference sample collected
Ar_Ar	X, sample age determined by argon-argon ($^{40}Ar/^{39}Ar$) geochronology (this report and Cosca and Morgan, 2018)
U_Pb	X, sample age determined by zircon uranium-lead (U-Pb) geochronology
K_Ar	X, sample age determined by potassium-argon (K-Ar) geochronology
Strat_Name	Stratigraphic unit name (Bonham and Garside, 1979; Ashley, 1974; 1979; 1990a)
Ign_Form	Form (lava, ash-flow tuff, plug, stock, and so forth) of the igneous rock represented by each sample

Table 2. Definition and characterization of data fields included in appendix 2 (petrographic data).

Field name	Field description
Field_ID	Field-assigned sample identifier; Field_ID entries link data for individual rows to the contents of particular rows in the other appendixes and, for U.S. Geological Survey samples, to the National Geochemical Database
Unit	Stratigraphic unit name (Bonham and Garside, 1979; Ashley, 1974; 1979; 1990a); repeated in this appendix to enable data sorting by unit name
AbdQtz	Microscope-based estimate of abundance of quartz phenocrysts relative to the whole rock, in volume percent. TR, trace (<0.5 volume percent) amounts
AbdAlkFld	Microscope-based estimate of abundance of alkali feldspar phenocrysts relative to the whole rock, in volume percent. TR, trace (<0.5 volume percent) amounts
AbdPl	Microscope-based estimate of abundance of plagioclase phenocrysts relative to the whole rock, in volume percent. TR, trace (<0.5 volume percent) amounts
AbdHbl	Microscope-based estimate of abundance of hornblende phenocrysts relative to the whole rock, in volume percent. TR, trace (<0.5 volume percent) amounts
AbdBt	Microscope-based estimate of abundance of biotite phenocrysts relative to the whole rock, in volume percent. TR, trace (<0.5 volume percent) amounts
AbdPx	Microscope-based estimate of abundance of pyroxene phenocrysts relative to the whole rock, in volume percent. TR, trace (<0.5 volume percent) amounts
Cpx_Opx	Presence of clinopyroxene (C) and orthopyroxene (O); if both are present, then letter designation for dominant pyroxene is uppercase, and letter designation for subordinate pyroxene follows in lower case; if both are capitalized the two pyroxenes are approximately equally abundant
AbdOl	Microscope-based estimate of abundance of olivine phenocrysts relative to the whole rock, in volume percent. TR, trace (<0.5 volume percent) amounts
AbdOpq	Microscope-based estimate of abundance of opaque iron-titanium oxide minerals relative to the whole rock, in volume percent. TR, trace (<0.5 volume percent) amounts
TotXls	Microscope-based estimate of total phenocryst content relative to the whole rock, in volume percent. TR, trace (<0.5 volume percent) amounts
ClrIndx	Microscope-based estimate of color index (sum of the abundances of hornblende, biotite, pyroxene, olivine, and opaque iron-titanium oxide minerals) in volume percent. TR, trace (<0.5 volume percent) amounts
AgsQtz	Microscope-based estimate of average grain size of quartz phenocrysts, in millimeters
AgsAlkFld	Microscope-based estimate of average grain size of alkali feldspar phenocrysts, in millimeters
AgsPl	Microscope-based estimate of average grain size of plagioclase phenocrysts, in millimeters
AgsHbl	Microscope-based estimate of average grain size of hornblende phenocrysts, in millimeters
AgsBt	Microscope-based estimate of average grain size of biotite phenocrysts, in millimeters
AgsPx	Microscope-based estimate of average grain size of pyroxene phenocrysts, in millimeters
AgsOl	Microscope-based estimate of average grain size of olivine phenocrysts, in millimeters
AgsOpq	Microscope-based estimate of average grain size of opaque iron-titanium oxide crystals, in millimeters

Table 2. Definition and characterization of data fields included in appendix 2 (petrographic data).—Continued

Field name	Field description
MgsQtz	Microscope-based estimate of maximum grain size (length) of largest quartz phenocryst, in millimeters
MgsAlkFld	Microscope-based estimate of maximum grain size (length) of largest alkali feldspar phenocryst, in millimeters
MgsPl	Microscope-based estimate of maximum grain size (length) of largest plagioclase phenocryst, in millimeters
MgsHbl	Microscope-based estimate of maximum grain size (length) of largest hornblende phenocryst, in millimeters
MgsBt	Microscope-based estimate of maximum grain size (length) of largest biotite phenocryst, in millimeters
MgsPx	Microscope-based estimate of maximum grain size (length) of largest pyroxene phenocryst, in millimeters
MgsOl	Microscope-based estimate of maximum grain size (length) of largest olivine phenocryst, in millimeters
MgsOpq	Microscope-based estimate of maximum grain size (length) of largest opaque iron-titanium oxide crystal, in millimeters
Texture	Characteristic petrographic textures as determined by microscopic observation—abbreviations: A, aphyric; F, fragmental; FL, flow laminated; H, hyalophitic; I, intersertal; IG, intergranular; P, porphyritic; PT, pilotaxitic; T, trachytic; V, vesicular
AccessMnrls	Accessory minerals identified by microscopic observation; listed in order of decreasing abundance—abbreviations: Aln, allanite; Ap, apatite; Ttn, titanite; Zrn, zircon
XlQtz	Microscope-based estimate of crystallinity of quartz phenocrysts—abbreviations: A, anhedral; S, subhedral; E, euhedral. If more than one crystallinity type is present, the dominant form is listed first
XlAlkFld	Microscope-based estimate of crystallinity of alkali feldspar phenocrysts—abbreviations: A, anhedral; S, subhedral; E, euhedral. If more than one crystallinity type is present, the dominant form is listed first
XlPl	Microscope-based estimate of crystallinity of plagioclase phenocrysts—abbreviations: A, anhedral; S, subhedral; E, euhedral. If more than one crystallinity type is present, the dominant form is listed first
XlHbl	Microscope-based estimate of crystallinity of hornblende phenocrysts—abbreviations: A, anhedral; S, subhedral; E, euhedral. If more than one crystallinity type is present, the dominant form is listed first
XlBt	Microscope-based estimate of crystallinity of biotite phenocrysts—abbreviations: A, anhedral; S, subhedral; E, euhedral. If more than one crystallinity type is present, the dominant form is listed first
XlPx	Microscope-based estimate of crystallinity of pyroxene phenocrysts—abbreviations: A, anhedral; S, subhedral; E, euhedral. If more than one crystallinity type is present, the dominant form is listed first
XlOl	Microscope-based estimate of crystallinity of olivine phenocrysts—abbreviations: A, anhedral; S, subhedral; E, euhedral. If more than one crystallinity type is present, the dominant form is listed first
XlOpq	Microscope-based estimate of crystallinity of opaque iron-titanium oxide phenocrysts—abbreviations: A, anhedral; S, subhedral; E, euhedral. If more than one crystallinity type is present, the dominant form is listed first
Petrog_Com	Groundmass (gndms) characteristics and any other noteworthy features; the degree to which hornblende (Hbl) and biotite (Bt) are oxidized is also noted
HblClr	Pleochroic colors of hornblende phenocrysts, if present
AltExtnt	Microscope-based estimate of the extent of alteration where 1 indicates a completely fresh sample and 5 indicates a completely altered sample in which primary textures and minerals are not identifiable; intermediate values of 2 through 4 identify progressively more altered samples

Table 3. Definition and characterization of data fields included in appendix 3 (geochemical data).

Field name	Field description
Field_ID	Field-assigned sample identifier; Field_ID entries link data for individual rows to the contents of particular rows in the other appendixes and, for U.S. Geological Survey samples, to the National Geochemical Database
Strat_Name	Stratigraphic unit name (Bonham and Garside, 1979; Ashley, 1974; 1979; 1990a); repeated in this appendix to enable data sorting by unit name
SiO2_pct	Silicon, as silicon dioxide, in weight percent; recalculated to 100 percent on a volatile-free basis
TiO2_pct	Titanium, as titanium dioxide, in weight percent; recalculated to 100 percent on a volatile-free basis
Al2O3_pct	Aluminum, as aluminum trioxide, in weight percent; recalculated to 100 percent on a volatile-free basis
FeO_pct	Total iron, as ferrous oxide, in weight percent; recalculated to 100 percent on a volatile-free basis
MnO_pct	Manganese, as manganese oxide, in weight percent; recalculated to 100 percent on a volatile-free basis
MgO_pct	Magnesium, as magnesium oxide, in weight percent; recalculated to 100 percent on a volatile-free basis
CaO_pct	Calcium, as calcium oxide, in weight percent; recalculated to 100 percent on a volatile-free basis
Na2O_pct	Sodium, as sodium oxide, in weight percent; recalculated to 100 percent on a volatile-free basis
K2O_pct	Potassium, as potassium oxide, in weight percent; recalculated to 100 percent on a volatile-free basis
P2O5_pct	Phosphorus, as phosphorus pentoxide, in weight percent; recalculated to 100 percent on a volatile-free basis
LOI_pct	Volatile content lost on ignition, in weight percent
H2O+(b)_pct	Structurally bound or essential water, in weight percent
H2O-(m)_pct	Nonessential moisture, in weight percent
CO2_pct	Carbon dioxide, in weight percent
F_pct	Fluoride, in weight percent
Total_I_pct	Initial, prerecalculation sum of oxide abundances, in weight percent
Volatile_pct	Total volatile content, in weight percent; calculated as the sum of bound water, moisture, carbon dioxide, and fluorine or as the content lost on ignition
Ba_ppm	Barium, in parts per million
Be_ppm	Beryllium, in parts per million
Cs_ppm	Cesium, in parts per million
Rb_ppm	Rubidium, in parts per million
Sr_ppm	Strontium, in parts per million
Y_ppm	Yttrium, in parts per million
Zr_ppm	Zirconium, in parts per million
Hf_ppm	Hafnium, in parts per million
Nb_pct	Niobium, in parts per million
Th_ppm	Thorium, in parts per million
U_ppm	Uranium, in parts per million
Ga_ppm	Gallium, in parts per million
La_ppm	Lanthanum, in parts per million

Table 3. Definition and characterization of data fields included in appendix 3 (geochemical data).—Continued

Field name	Field description
Ce_ppm	Cerium, in parts per million
Pr_ppm	Praseodymium, in parts per million
Nd_ppm	Neodymium, in parts per million
Sm_ppm	Samarium, in parts per million
Eu_ppm	Europium, in parts per million
Gd_ppm	Gadolinium, in parts per million
Tb_ppm	Terbium, in parts per million
Dy_ppm	Dysprosium, in parts per million
Ho_ppm	Holmium, in parts per million
Er_ppm	Erbium, in parts per million
Tm_ppm	Thulium, in parts per million
Yb_ppm	Ytterbium, in parts per million
Lu_ppm	Lutetium, in parts per million
Ag_ppm	Silver, in parts per million
Au_ppm	Gold, in parts per million
Co_ppm	Cobalt, in parts per million
Cr_ppm	Chromium, in parts per million
Ni_ppm	Nickel, in parts per million
Sc_ppm	Scandium, in parts per million
V_ppm	Vanadium, in parts per million
Cu_ppm	Copper, in parts per million
Mo_ppm	Molybdenum, in parts per million
Pb_ppm	Lead, in parts per million
Zn_ppm	Zinc, in parts per million
Sn_ppm	Tin, in parts per million
W_ppm	Tungsten, in parts per million
Ta_ppm	Tantalum, in parts per million
As_ppm	Arsenic, in parts per million
Sb_ppm	Antimony, in parts per million
B_ppm	Boron, in parts per million
chem_src	Source of geochemical data: 1, U.S. Geological Survey, National Geochemical Database, 2013; 2, samples collected by Ashley, R.P., U.S. Geological Survey, data presented in this report; 3, samples collected by du Bray, E.A., U.S. Geological Survey, data presented in this report; 4, Ransome (1909); 5, Knopf (1918); 6, Bonham and Garside (1979); 7, samples collected by Vikre, P.G., U.S. Geological Survey, data presented in this report. For a few samples, data were culled from two or more sources; for example, major oxide data may have been compiled from one source and trace element data from another

References Cited

Albers, J.P., and Stewart, J.H., 1972, Geology and mineral deposits of Esmeralda County, Nevada: Nevada Bureau of Mines and Geology Bulletin 78, 80 p.

Ashley, R.P., 1974, Goldfield mining district: Nevada Bureau of Mines and Geology Report 19, p. 49–66.

Ashley, R.P., 1979, Relation between volcanism and ore deposition at Goldfield, Nevada: Nevada Bureau of Mines and Geology Report 33, p. 77–86.

Ashley, R.P., 1990a, The Goldfield gold district, Esmeralda and Nye Counties, Nevada, *in* Shawe, D.R., and Ashley, R.P., eds., Epithermal gold deposits—Part 1: U.S. Geological Survey Bulletin 1857–H, p. H1–H7.

Ashley, R.P., 1990b, The Tonopah precious-metal district, Esmeralda and Nye Counties, Nevada, *in* Shawe, D.R., and Ashley, R.P., eds., Epithermal gold deposits—Part 1: U.S. Geological Survey Bulletin 1857–H, p. H8–H13.

Ashley, R.P., and Albers, J.P., 1975, Distribution of gold and other ore-related elements near ore bodies in the oxidized zone at Goldfield, Nevada: U.S. Geological Survey Professional Paper 843–A, 48 p.

Ashley, R.P., and Silberman, M.L., 1976, Direct dating of mineralization at Goldfield, Nevada by potassium-argon and fission-track methods: Economic Geology, v. 71, p. 904–924.

Barth A.P., and Wooden J.L., 2010, Coupled elemental and isotopic analyses of polygenetic zircons from granitic rocks by ion microprobe, with implications for melt evolution and the sources of granitic magmas: Chemical Geology, v. 277, p. 149–159.

Black, L.P., Kamo, S.L., Allen, C.M., Davis, D.W., Aleinikoff, J.N., Valley, J.W., Mudil, R., Campbell, I.H., Korsch, R.J., Williams, I.S., and Foudoulis, C., 2004, Improved 206Pb/238U microprobe geochronology by the monitoring of a trace-element-related matrix effect; SHRIMP, ID-TIMS, ELA-ICPMS and oxygen isotope documentation for a series of zircon standards: Chemical Geology, v. 205, p. 115–140. [Also available at https://doi.org/10.1016/j.chemgeo.2004.01.003.]

Blakely, R.J., John, D.A., Box, S.E., Berger, B.R., Fleck, R.J., Ashley, R.P., and Heinemeyer, G.R., 2007, Crustal controls on magmatic-hydrothermal systems; a geophysical comparison of White River, Washington, with Goldfield, Nevada: Geosphere, v. 3, p. 91–107.

Bonham, H.F., Jr., and Garside, L.J., 1974, Tonopah mining district and vicinity: Nevada Bureau of Mines and Geology Report 19, p. 42–48.

Bonham, H.F., Jr., and Garside, L.J., 1979, Geology of the Tonopah, Lone Mountain, Klondike, and northern Mud Lake quadrangles, Nevada: Nevada Bureau of Mines and Geology Bulletin 92, 142 p.

Colgan, J.P., Egger, A.E., John, D.A., Cousens, B., Fleck, R.J., and Henry, C.D., 2011, Oligocene and Miocene arc volcanism in northeastern California: Evidence for post-Eocene segmentation of the subducting Farallon plate: Geosphere, v. 7, p. 733–755.

Colgan, J.P., 2018, Zircon U-Pb age and trace element data for Cenozoic igneous rocks in the Tonopah area, Nevada: U.S. Geological Survey data release, https://doi.org/10.5066/P9FVS0UK.

Cosca, M.A., and Morgan, L.E., 2018, $^{40}Ar/^{39}Ar$ geochronology of the Tonopah, Divide, and Goldfield districts, Nevada: U.S. Geological Survey data release, accessed June 2, 2018 at https://doi.org/10.5066/F7833R8Z.

Crafford, A.E.J., 2007, Geologic Map of Nevada: U.S. Geological Survey Data Series 249, 1 CD-ROM, 46 p., 1 plate. [Also available online at http://pubs.usgs.gov/ds/2007/249/.]

Crafford, A.E.J., 2008, Paleozoic tectonic domains of Nevada: An interpretive discussion to accompany the geologic map of Nevada: Geosphere, v. 4, p. 260–291.

du Bray, E.A., John, D.A., Vikre, P.G., Colgan, J.P., Cosca, M.A., Morgan, L.E., Fleck, R.J., Premo, W.R., Holm-Denoma, C.S., and Heizler, M.T., 2019, Data to accompany U.S. Geological Survey Data Series 1099: Petrographic, geochemical, and geochronologic data for Cenozoic volcanic rocks of the Tonopah, Divide, and Goldfield mining districts, Nevada: U.S. Geological Survey data release, https://doi.org/10.5066/P9HZCRGV.

du Bray, E.A., John, D.A., and Cousens, B.L., 2014, Petrologic, tectonic, and metallogenic evolution of the southern segment of the ancestral Cascades magmatic arc, California and Nevada: Geosphere, v. 10, p. 1–39, accessed December 15, 2014 at https://doi.org/10.1130/GES00944.1.

Erdman, C.P., and Barabas, A.H., 1996, Precious metal mineralization at Gold Mountain, Tonopah Divide district, Esmeralda County, Nevada, *in* Coyner, A.R, and Fahey, P.L., eds., Geology and Ore Deposits of the American Cordillera Symposium Proceedings: Reno, Geological Society of Nevada, p. 329–351.

Gehrels, G., 2012, Detrital zircon U-Pb geochronology—Current methods and new opportunities, *in* Busby, C., and Azor, A., eds., Tectonics of sedimentary basins—Recent advances: Wiley-Blackwell Publishing, p. 47–62, https://doi.org/10.1002/9781444347166.ch2.

Gill, J., 1981, Orogenic andesites and plate tectonics: New York, Springer-Verlag, 390 p.

Graney, J.R., 1987, Hasbrouck Mountain, Nevada—Precious-metal mineralization in a fossil hot springs environment, *in* Johnson, J.L., ed., Bulk mineable precious metal deposits of the western United States, guidebook for field trips: Reno, Geological Society of Nevada, p. 120–125.

Heizler, Matt, 2003, $^{40}Ar/^{39}Ar$ geochronology results from Peter Vikre samples: New Mexico Geochronological Research Laboratory Internal Report NMGRL-IR-374&397, 10 p.

Heizler, Matt, 2005, $^{40}Ar/^{39}Ar$ geochronology results from Peter Vikre samples: New Mexico Geochronological Research Laboratory Internal Report NMGRL-IR-466, 16 p.

Hu, Z., Gao, S., Liu, Y., Hu, S., Chen, H., and Yuan, H., 2008, Signal enhancement in laser ablation ICP–MS by addition of nitrogen in the central channel gas: Journal of Analytical Atomic Spectrometry, v. 23, p. 1093–1101.

Ireland, T.R., and Williams, I.S., 2003, Considerations in zircon geochronology by SIMS, *in* Hanchar, J.M., and Hoskin, P.W.O., eds., Zircon: Mineralogical Society of America and Geochemical Society, Reviews in Mineralogy and Geochemistry, v. 53, p. 215–241.

John, D.A., du Bray, E.A., Blakely, R.J., Fleck, R.J., Vikre, P.G., Box, S.E., and Moring, B.C., 2012, Miocene magmatism in the Bodie Hills volcanic field, California and Nevada—A long-lived eruptive center in the southern segment of the ancestral Cascades arc: Geosphere, v. 8, p. 44–97.

John, D.A., du Bray, E.A., Henry, C.D., and Vikre, P.G., 2015, Cenozoic magmatism and epithermal gold-silver deposits of the southern ancestral Cascade arc, western Nevada and eastern California *in* Pennell, W.M., and Garside, L.J., eds., New Concepts and Discoveries: Geological Society of Nevada Symposium Proceedings, May 2015, Sparks, Nevada, p. 611–645.

John, D.A., and McKee, E.H.,1987, K-Ar ages of granitic plutonism and hydrothermal alteration in western part of the Tonopah 1° by 2° quadrangle, Nevada: Isochron/West, no. 48, p. 16–18.

Knopf, Adolph, 1918, Geology and ore deposits of the Yerington district, Nevada: U.S. Geological Survey Professional Paper 114, 68 p.

Kuiper, K.F., Deino, A., Hilgen, F.J., Krijgsman, W., Renne, P.R., and Wijbrans, J.R., 2008, Synchronizing rock clocks of Earth history: Science, v. 320, p. 500–504.

Lee, J.-Y., Marti, K., Severinghaus, J.P., Kawamura, K., Yoo, H.-S., Lee, J.B., and Kim, J.S., 2006, A redetermination of the isotopic abundances of atmospheric Ar: Geochimica et Cosmochimica Acta, v. 70, p. 4507–4512.

Ludwig, K.R., 2003, Isoplot 3.00, a geochronological tool-kit for Excel: Berkeley Geochronology Center Special Publication 4, 67 p.

Ludwig, K.R., 2009, SQUID 2—A User's Manual, rev. 12 Apr. 2009: Berkeley Geochronology Center Special Publication No. 5.

Ludwig, K.R., 2012, Isoplot 3.75—A geochronological toolkit for Microsoft Excel: Berkeley Geochronology Center Special Publication, v. 5, 75 p.

Mattinson, J.M., 2010, Analysis of the relative decay constants of ^{235}U and ^{238}U by multi step CA-TIMS measurements of closed-system natural zircon samples: Chemical Geology, v. 275, p. 186–198.

Min, Kyoungwon, Mundil, Roland, Renne, P.R., and Ludwig, K.R., 2000, A test for systematic errors in $^{40}Ar/^{39}Ar$ geochronology through comparison with U/Pb analysis of a 1.1-Ga rhyolite: Geochimica et Cosmochimica Acta, v. 64, p. 73–98.

Nolan, T.B., 1935, Underground geology of the Tonopah mining district, Nevada: Nevada University Bulletin 29, no. 5, 49 p.

Paton, C., Hellstrom, J., Paul, B., Woodhead, J., and Hergt, J., 2011, Iolite: freeware for the visualization and processing of mass spectrometric data: Journal of Analytical Atomic Spectrometry, v. 26, p. 2508–2518., https://doi.org/10.1039/C1JA10172B.

Ransome, F.L., 1909, The geology and ore deposits of Goldfield, Nevada: U.S. Geological Survey Professional Paper 66, 258 p.

Sláma, J., Košler, J., Condon, D.J., Crowely, J.L., Gerdes, A., Hanchar, J.M., Horstwood, M.S.A., Morris, G.A., Nasdala, L., Norberg, N., Schaltegger, U., Schoene, B., Tubrett, M.N., Whitehouse, M.J., 2008, Plesovice zircon—A new natural reference material for U-Pb and Hf isotopic microanalysis: Chemical Geology, v. 249, p. 1–35. https://doi.org/10.1016/j.chemgeo.2007.11.005.

Stacey, J.S. and Kramers, J.D., 1975, Approximation of terrestrial lead isotope evolution by a two-stage model: Earth and Planetary Science Letters, v. 26, p. 207–221.

Steiger, R.H., and Jäger, E., 1977, Subcommission on geochronology—Convention on the use of decay constants in geo- and cosmochronology: Earth and Planetary Science Letters, v. 36, p. 359–362.

Taggart, J.E., Jr., 2002, Analytical methods for chemical analysis of geologic and other materials: U.S. Geological Survey Open-File Report 02–0223, available online at http://pubs.usgs.gov/of/2002/ofr-02-0223/OFR-02-0223.pdf.

Taylor, J.R., 1982, An introduction to error analysis—The study of uncertainties in physical measurements: Mill Valley, California, University Science Books, 270 p.

Vikre, P.G., and Henry, C.D., 2011, Quartz-alunite alteration cells in the ancestral southern Cascades magmatic arc, *in* Steininger, R., and Pennell, B., eds., Great Basin evolution and metallogeny: Proceedings, Geological Society of Nevada, 2010 Symposium Reno, Nevada, p. 701–745.

Williams, I.S., 1997, U-Th-Pb geochronology by ion microprobe: not just ages but histories: Society of Economic Geologists Reviews in Economic Geology, v. 7, p. 1–35.

Appendixes 1 through 10 are tables and can be accessed at https://doi.org/10.3133/ds1099

Appendix 1. Status and Treatment of Samples from the Tonopah, Divide, and Goldfield Mining Districts.

Appendix 2. Petrographic Data for Samples from the Tonopah, Divide, and Goldfield Mining Districts.

Appendix 3. Geochemical Data for Rock Samples from the Tonopah, Divide, and Goldfield Mining Districts.

Appendix 4. $^{40}Ar/^{39}Ar$ Geochronologic Data for Samples from the Tonopah, Divide, and Goldfield Mining Districts Obtained in the U.S. Geological Survey $^{40}Ar/^{39}Ar$ Laboratory in Denver, Colorado.

Appendix 5. Summary of New $^{40}Ar/^{39}Ar$ Age Determinations for Samples from the Tonopah, Divide, and Goldfield Mining Districts Obtained in the U.S. Geological Survey $^{40}Ar/^{39}Ar$ Laboratory in Denver, Colorado.

Appendix 6. $^{40}Ar/^{39}Ar$ Geochronologic Data for Samples from the Goldfield Mining District Obtained in the New Mexico Geochronological Research Laboratory.

Appendix 7. $^{40}Ar/^{39}Ar$ Geochronologic Data for Samples from the Goldfield Mining District Obtained in the U.S. Geological Survey $^{40}Ar/^{39}Ar$ Laboratory in Menlo Park, California.

Appendix 8. Sensitive High Resolution Ion Microprobe (SHRIMP) Zircon U-Pb Geochronologic Data for Rock Samples from the Tonopah, Divide, and Goldfield Mining Districts.

Appendix 9. Laser Ablation ICP-MS Zircon U-Pb Geochronologic Data for Rock Samples from the Tonopah, Divide, and Goldfield Mining Districts.

Appendix 10. Results of Point Counts for Samples of the Fraction Tuff and Heller Tuff from the Tonopah and Divide Mining Districts.

Geology, Geophysics, and Geochemistry Science Center

Publishing support provided by the Science Publishing Network, Denver and West Trenton Publishing Service Centers

For more information concerning the research in this report, contact the
Center Director, USGS Geology, Geophysics, and Geochemistry Science Center

Box 25046, Mail Stop 973
Denver, CO 80225
(303) 236-1800

Or visit Geology, Geophysics, and Geochemistry Science Center website at
https://www.usgs.gov/centers/gggsc

ISSN 2327-638X (online)
https://doi.org/10.3133/ds1099